



Solid Flow Regimes Within Dry Sliding Contacts

Guilhem Mollon¹

Received: 7 June 2019 / Accepted: 30 September 2019
© Springer Science+Business Media, LLC, part of Springer Nature 2019

Abstract

In this paper, we investigate the regimes of velocity accommodation and of load transmission within a dry sliding interface, in the presence of a solid and discontinuous interfacial layer (the so-called third body). To that end, an appropriate numerical framework called the multibody meshfree approach is used to implement a local model of such an interface, and a comprehensive dimensionless parametric study is performed in order to analyse the influence of the mechanical properties of the third body on the interfacial solid flow regimes, on the friction coefficient, and on the modes of energy dissipation. To that end, the concept of partial coefficient of friction is introduced. The numerical results demonstrate that the friction in the interface is limited by changes in the kinematics of the shear accommodation in the third-body layer and by the activation of different modes of energy dissipation (related either to surface area creation/destruction in the third-body layer or to bulk deformation of the solid matter composing it) which are uncorrelated in the parametric space of the mechanical properties of the third-body particles.

Keywords Friction · Contact · Third body · Soft grains · Shearing · Flow regimes

1 Introduction

Most mechanical systems exhibit contacts, which may be either dry or lubricated depending on a large number of engineering constraints. While the theory of friction in the presence of fluid lubrication has now reached a form of maturity and seeks for more and more accurate quantitative predictions, the case of dry contacts remains much more uncertain. In many practical situations, this is problematic because dry friction constitutes a large part of the boundary conditions of continuum mechanics (even in the case of tight mechanical assemblies such as bolted joints, see [1]). Modern theories of dry friction often focus on geometric features: friction is explained by the roughness of the surfaces put into contact and by the welding, yielding, and dynamics of asperities sliding past each other [2], at several entangled scales [3, 4]. A key quantity is the so-called real

contact area [5, 6], which is found to be much smaller than the nominal one and which makes it possible to derive the classical Amontons–Coulomb linear friction law based on a limited set of assumptions [7].

This framework has the merit of the simplicity, but sometimes fails to predict experimental friction results, mostly for two reasons: (i) it neglects the intrinsically multi-scale character of dry friction and (ii) it only applies to clean and fresh contacts where the notion of asperity has a clear geometrical meaning. This observation led to the development of alternative, less quantitative, and more phenomenological approaches, the most prominent one being that of the tribological triplet [8]. This conceptual framework, mostly built after close experimental observations of engineering contacts in a practical context, states that one cannot understand and predict the behaviour of a real dry contact without considering three different scales. The intermediate scale is obviously that of the two solid bodies into contact (called “first bodies” in this framework), including their geometry, roughness, deformability, damage, wear, etc. For that scale, such tools as contact mechanics [9] and continuum mechanics [10, 11] are commonly used. The upper scale is that of the mechanical system into which the first bodies take place, including its own loadings, dynamics, inertias, stiffness, damping, actuators, etc. That scale can be handled properly

Electronic supplementary material The online version of this article (<https://doi.org/10.1007/s11249-019-1233-0>) contains supplementary material, which is available to authorized users.

✉ Guilhem Mollon
guilhem.mollon@insa-lyon.fr

¹ Université de Lyon, LaMCoS, INSA-Lyon, CNRS
UMR5259, 69621 Lyon, France

using common tools of linear and nonlinear dynamics [12]. The third scale is that of the layer of solid matter which is very often observed in real contacts, provided that they are sufficiently loaded and mature enough. This layer generally originates from the degradation of the surfaces put into contact, but not always [13], and is called “third body” because experimental evidence shows that it behaves differently from the first bodies which created it [14]. While the two larger scales can be simulated with existing approaches, the third body has remained much more challenging to simulate numerically, for several reasons. The first one is that it can exhibit a large variety of aspects (e.g. granular, plastic, brittle, platelets, etc. [15]), and there is no evidence that a single framework could reproduce (let alone predict) all these behaviours. The second reason is that the typical thickness of this layer (around the micrometre, usually) makes it too large to apply first-principles simulations. The third one is related to the complicated kinematics of this interfacial layer during sliding, which certainly prevent the use of classical meshed continuum-based numerical frameworks. The fourth reason is that, even if such continuum-based method existed, the proper constitutive law to apply to this layer would still be unknown. And yet, since the surfaces of the first bodies do not touch any more when it is well established, this layer controls friction, and the question of its rheology cannot be eluded.

This led to the development of dedicated numerical approaches, outside of the framework of continuum mechanics. Discrete element methods (DEMs) were first used by [16], followed and further developed by a large number of studies in the past 15 years [17–20] (see [21] for a full account). DEM was primarily developed in the geomechanics community [22] and is nowadays commonly used in granular mechanics, civil and mechanical engineering, and granular physics [23–26]. When this approach is used in a tribological framework, the third body is represented by a large set of rigid particles which interact by the means of contacts, with prescribed (usually cohesive) interaction laws. It has been successful to reproduce several key phenomena, such as sliding localization [27] or wear patterns [28], but remains limited by its most prominent assumption, i.e. by the fact that the grains are perfectly rigid. Indeed, this assumption leads the simulated third bodies to behave mostly in a granular way, meaning that the rheology of the layer is mostly driven by the steric exclusion of the geometrical shapes of the grains. There is thus no evidence that such approach is capable of reproducing the large variety of behaviours which are observed experimentally in real tribological triplets. In this paper, we explore the range of behaviours that arise when the individual grains composing the third-body layer are allowed to deform. In contrast to the flow regimes in the cases of dry granular flows [29] and of granular suspensions [30], which have been extensively studied in the fields of granular physics and rheophysics, this class of divided solid

matter remains to date rather unexplored. We demonstrate that this additional property allows the spontaneous emergence of a large number of solid flow regimes within the interface, which control in a large proportion the local value of the friction coefficient.

Several benefits may be expected from a more accurate modelling of the third-body flow within the interface. At the moment, the only way we have to understand what happens in such a contact is to open it and observe the surfaces with appropriate tools (optic microscopy, SEM, EDX, etc.). It is only a post-mortem view, and the processes that led to the observed state are left to speculation. Many experimentalists often regret this lack of in situ view, and numerical simulation is an interesting alternative. A numerical tool making it possible to relate post-mortem observations to the local behaviours that created the observed state might improve our understanding of tribological scenarios. It could also provide some way to understand and predict wear by analysing more closely the interactions between the third body and the surfaces of the first bodies, since some flow regimes may be more aggressive to the surface than others. As a long-term purpose, a local numerical simulation may allow to understand in what ways the properties of the matter composing the third-body layer allow it to self-organize in order to oppose a resistance to shearing. It may make it possible to design coatings in order to target a desirable flow regime for specific friction and wear purposes. It might also enhance our understanding of dry friction in general, with the possible perspective of writing predictive dry friction laws based on local considerations of energetic principles.

In “**Methods**” section, the methods used in this study are presented, including successively an overview of the numerical framework, details on the performed numerical simulations, and a description of the relevant dimensionless parameters and of the investigated parametric space. In “**Results**” section, the numerical results are presented. Friction coefficient is studied first, and a particular focus is then put on the flow regimes obtained for seven particularly relevant simulations extracted from the parametric study. This section ends with a thorough investigation of the energy dissipation modes in the interface. “**Discussion**” section provides a discussion on the links between the flow regime in the interface, the fabric of the third body, the modes of energy dissipation, and the friction coefficient. It provides a qualitative comparison with experimental results from the literature and concludes on the relevance of such numerical approach for future understanding of dry sliding contacts.

2 Methods

2.1 Numerical Framework

Classical DEM approaches consist in applying Newtonian dynamics to all the particles (called “grains”) of the sample, based on external forces (such as gravity) and on forces arising from contacts between them. In the early 2D implementations, grains were circular in order to simplify the computation of these contact forces. More recent implementations introduced the third dimension and the possibility of non-circular grains [31, 32], although the complexity brought by these features unfortunately limits their use in the different scientific communities interested in this technique. Introducing deformable grains in this context, however, is not straightforward. Early attempts were made to use commercial finite-element method (FEM) codes capable of handling both deformable bodies and complicated (and evolving) contact geometries [33, 34], but they were limited by the fact that FEM codes are not designed to handle large collections of individual bodies.

The numerical framework used in the present paper is called the multibody meshfree approach. It was developed primarily for tribological purposes and is implemented in an open-source code called MELODY_2D. It combines the features of typical FEM tools (i.e. the notion of a stress–strain relation controlling the deformation of a given body based on the loadings it is submitted to) and of DEM tools (i.e. the ability to handle the interactions between a large number of bodies in motion, with complicated shapes). To that end, each grain is discretized by a number of so-called field nodes, each of which carrying two degrees of freedom in displacement. The code is currently limited to plane-strain kinematics. In the solid domains between these field nodes, the displacement field is interpolated using moving least square (MLS) meshfree shape functions, in a manner close (but not identical) to the element-free Galerkin (EFG) framework [35, 36]. A weak formulation along with a classical quadrature numerical integration is used to evaluate the stress fields within all the discretized grains, based on their strain fields. Finite strains are of course accounted for since the grains are expected to be submitted to complex motions and large deformations. The use of meshfree shape functions instead of typical FEM shape functions brings a number of benefits, not the least being a much larger robustness to very large deformations of the grains thanks to the absence of mesh-related distortion issues. Apart from the shape functions, this method is very close to classical FEM.

The field nodes located on the external border of a given grain are linked by segments, which thus form the

discretized piecewise linear contour of this grain. This contour is used to deal with contacts between grains, based on a robust penalty-based two-way contact algorithm. The most interesting part of such a contact modelling is that the strength of a contact between two grains depends on the spatial extension of this contact (namely, its length, in a 2D context), this extension being in turn a function of the local deformations of the grains. Hierarchical proximity detection is performed in order not to miss any contact. These proximity and contact algorithms are very close to those commonly used in polygonal DEM.

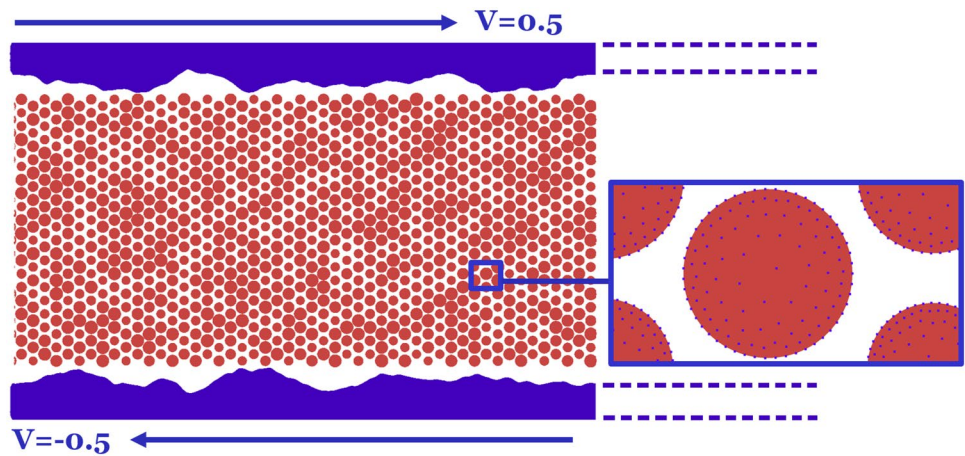
Because of the large number of strong nonlinearities of such a system (geometric, contact-related, and constitutive nonlinearities), an explicit solver is used to solve in a fully dynamic way the equations of motion of each degree of freedom of the system. A classical symplectic Euler scheme is used, like in classical DEM, but the time-stepping scheme of this solver is adaptive in order to avoid instabilities while optimizing the computational efficiency. The whole code is parallelized and exhibits a very good scaling in a shared memory architecture, thanks to its inherently divided nature. More details about the logic and implementation of this framework can be found in [37, 38]. Since classical DEM is just an end-member case of the more general multibody meshfree approach in the limit of infinitely rigid bodies, MELODY_2D can also perform DEM. It was used in that spirit to study the rheology of mixtures of rigid and deformable grains in a recent paper [39] and will be applied to a tribological analysis of solid flows in dry contacts in the remainder of the present paper.

2.2 Numerical Model

In order to investigate the way a discontinuous and compliant medium can accommodate a velocity gradient, transmit vertical load, and control friction, a theoretical model is proposed in this subsection. In this model, two rigid bodies are considered, in order to represent a local patch within a contact between two surfaces. These first bodies are generated with a self-affine roughness and exhibit an RMS equal to 1 for a length $L = 100$. (The study is dimensionless, so no intrinsic length unit is introduced.) Periodic boundary conditions are applied at their two extremities (Fig. 1). The two bodies are completely motion driven, meaning that they translate with respect to each other with a relative velocity $V = 1$ (the lower body travels leftwards at a velocity of $V/2$ and the upper body goes rightwards at a velocity of $V/2$), and at a constant gap called D .

The first bodies are separated by a collection of 2000 soft grains. In order to limit the number of assumptions, they are all circular in shape in their reference state. The average diameter of these grains is chosen to be equal to 1, and the sample is slightly polydisperse with diameters uniformly

Fig. 1 Sketch of the numerical model with rigid first bodies and deformable (and thus discretized) third-body particles



distributed between 0.85 and 1.15. Each grain is discretized by about 100–150 field nodes (Fig. 1), and a hyperelastic neo-Hookean constitutive model is applied to these grains in order to introduce their deformability up to very large strains in the simplest possible way. This model only has two parameters, the Young’s modulus E and the Poisson ratio ν . In order to prescribe a quasi-incompressibility, the Poisson ratio is set to 0.495 in all simulations. The density of all the matter introduced in the simulation is equal to 1.

In order to run such dynamic simulations, it is necessary to introduce a damping to the system. This is done using a classical Rayleigh damping (i.e. a damping matrix equal to the weighted sum of the mass and stiffness matrices), except that the weight attributed to the mass matrix is here taken as 0. The reason for this choice is that this part of the Rayleigh damping is frame dependent and therefore can only have a meaning in the case of structures which have a clear reference frame, which is not the case here. This means that the damping matrix is actually proportional to the stiffness matrix. The coefficient of proportionality is a user-defined parameter called α , with the dimension of a time. The resulting medium is very analogous to a Kelvin–Voigt viscoelastic solid. The chosen contact law is the same between two soft grains or between a soft grain and a first body: it is a cohesive contact law with a single parameter c which represents the strength per length unit of a contact between two surfaces. Hence, if a contact has a length equal to 1, c represents the force that is needed either to separate the two surfaces by pulling them apart (if applied in a tensile direction) or to trigger sliding between the two surfaces (if applied in a tangential direction).

2.3 Parametric Space

Since the first bodies are motion driven, both the normal and the tangential forces resulting from this motion are actually output quantities, which vary in time. Hence, a typical

simulation provides time series of normal force $F_n(t)$ and tangential force $F_t(t)$, and the resulting coefficient of friction can be obtained by the formula:

$$\mu = \bar{F}_n / \bar{F}_t \tag{1}$$

where \bar{F}_n and \bar{F}_t are the time averages of $F_n(t)$ and $F_t(t)$, respectively (Fig. 2). Besides, time-averaged normal and tangential stresses $\bar{\sigma}_n$ and $\bar{\sigma}_t$ are obtained by dividing \bar{F}_n and \bar{F}_t by the length L of the system.

In this study, we define three dimensionless quantities, which in turn define the parametric space that will be explored in the next section:

$$\tilde{E} = \log_{10} (E / \bar{\sigma}_n) \tag{2}$$

$$\tilde{c} = \log_{10} (c / \bar{\sigma}_n) \tag{3}$$

$$\tilde{\alpha} = \log_{10} (\alpha \cdot V / D) \tag{4}$$

The first one is a normalized stiffness (quantifying the degree of deformability of the third body with respect to

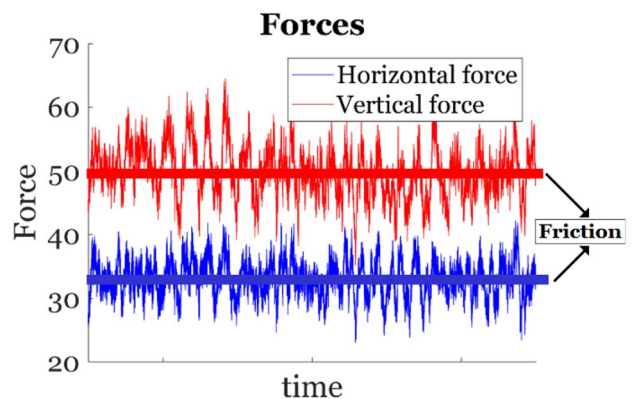


Fig. 2 Illustrative time series of total horizontal and vertical forces between the first bodies

the average stress it is submitted to), the second one is a normalized cohesion (quantifying the relative strength of the contacts within the system), and the third one is a normalized viscosity (quantifying the reluctance of the third body to accommodate high strain rates, with respect to the average one V/D applied to the whole layer, due to its Kelvin–Voigt-equivalent viscosity α). Logarithmic scales are used in order to represent in a clearer way the different orders of magnitude involved. In order to explore in a comprehensive manner this parametric space, 75 simulations are performed in the range $-0.15 \leq \tilde{E} \leq 1.2$, $-1 \leq \tilde{c} \leq 1.4$, and $-3.3 \leq \tilde{\alpha} \leq -1.5$.

Viscosity of solids is a complicated topic which is often overlooked in solid mechanics because its contribution to the mechanical response is negligible at common strain rates. However, solid matter in a third-body layer is exposed to very high shear rates, and the question of its viscosity (or at least of the viscous component of its viscoplastic response) should not be eluded. We can take the example of steel. If we assume a layer with a thickness of 10 μm and a sliding velocity of 1 m/s, we obtain an average strain rate of 10^5s^{-1} . (It can be much larger locally in the layer, depending on the flow regime.) For steel at such strain rates, literature ([40] and references therein) provides viscosity values in the range 10^3 to $10^5 \text{Pa} \cdot \text{s}$. For a Young's modulus of $\approx 200 \text{GPa}$ (and ignoring finite-strain nonlinear effects on the tangent value of this modulus), it leads to a Rayleigh α parameter in the range $5 \cdot 10^{-9} \text{s}$ to $5 \cdot 10^{-7} \text{s}$. In turn, injecting these α values and the corresponding layer thickness and sliding velocity in the expression of the dimensionless parameter $\tilde{\alpha}$, we get values in the range -3.3 to -1.3 , which is in very good agreement with the values used in the proposed parametric study. It is interesting to notice that the viscous stress induced by such viscosity at such strain rates is around the GPa, and possibly larger, meaning that it could become dominant when compared to the plastic stress.

The locations of the simulation points in the parametric space are shown in Fig. 3. For each simulation, a transient period is necessary in order to compact the sample (vertical motion of the first bodies) and to establish a solid flow regime (relative horizontal velocity of the two first bodies), and the obtained steady state is then simulated for a relative motion of the two bodies equal to 300. An observation of the friction signals showed that this duration was sufficient to obtain meaningful statistics. All quantitative results provided in the remainder of this paper are, if not stated otherwise, time averages on the whole duration of the steady-state sliding. Simulations were typically launched on 20 CPUs and took about two weeks each.

3 Results

3.1 Friction Coefficient

Figure 4 shows the coefficients of friction obtained for all the 75 simulations, as a function of the average normal stress (normalized by the Young's modulus). Interestingly, it appears that all the obtained values are in the range $0.13 < \mu < 1.08$. It means that these emerging friction values can be considered as quantitatively reasonable despite the fact that the parametric space of third-body physical properties where they were obtained is quite vast (more than one order of magnitude for \tilde{E} , more than two for \tilde{c} , and almost two for $\tilde{\alpha}$). It is, for example, quite striking to consider that, for the maximum value of \tilde{c} considered in this study, the cohesion is 25.2 times larger than the vertical stress, meaning that if two perfectly rigid and flat surfaces were simulated without third body, the friction coefficient would be equal to 25.2. It is clear from that observation that the presence of third body within the interface precludes a too large increase in the value of the coefficient of friction.

A better understanding is brought out by Fig. 5, where the value of the friction coefficient is interpolated in the whole parametric space $\{\tilde{E}, \tilde{c}, \tilde{\alpha}\}$. It is instructive to consider two slices of this space, corresponding to two values of $\tilde{\alpha}$. For a low value of the normalized viscosity ($\tilde{\alpha} = -3.2$), the coefficient of friction remains rather low (below 0.5) and seems to increase monotonically with the cohesion and the stiffness of the third body. However, for a high value of the normalized viscosity ($\tilde{\alpha} = -1.8$), the friction coefficient μ takes larger values (from 0.2 to 1.08) and exhibits a local maximum for a certain couple $\{\tilde{E}, \tilde{c}\}$ equal to $\{0.66, 0.96\}$. That point corresponds to a Young's modulus and a cohesion one order of magnitude larger than the applied vertical pressure, roughly speaking. This observation is counter-intuitive, since one would expect that an increase in the cohesion or of the stiffness of the grains would lead to an increase in the friction, like in the case of values of \tilde{E} and \tilde{c} lower than this point of maximum. Understanding the reason for this phenomenon requires a closer look at the flow regimes within the interface.

3.2 Flow Regimes

In this subsection, we pay a closer attention to seven simulations in particular. These simulations will be referred to using letters from A to G. Simulation A corresponds to a case for which the value of the friction is very low, while case C corresponds to a case of very large friction (almost

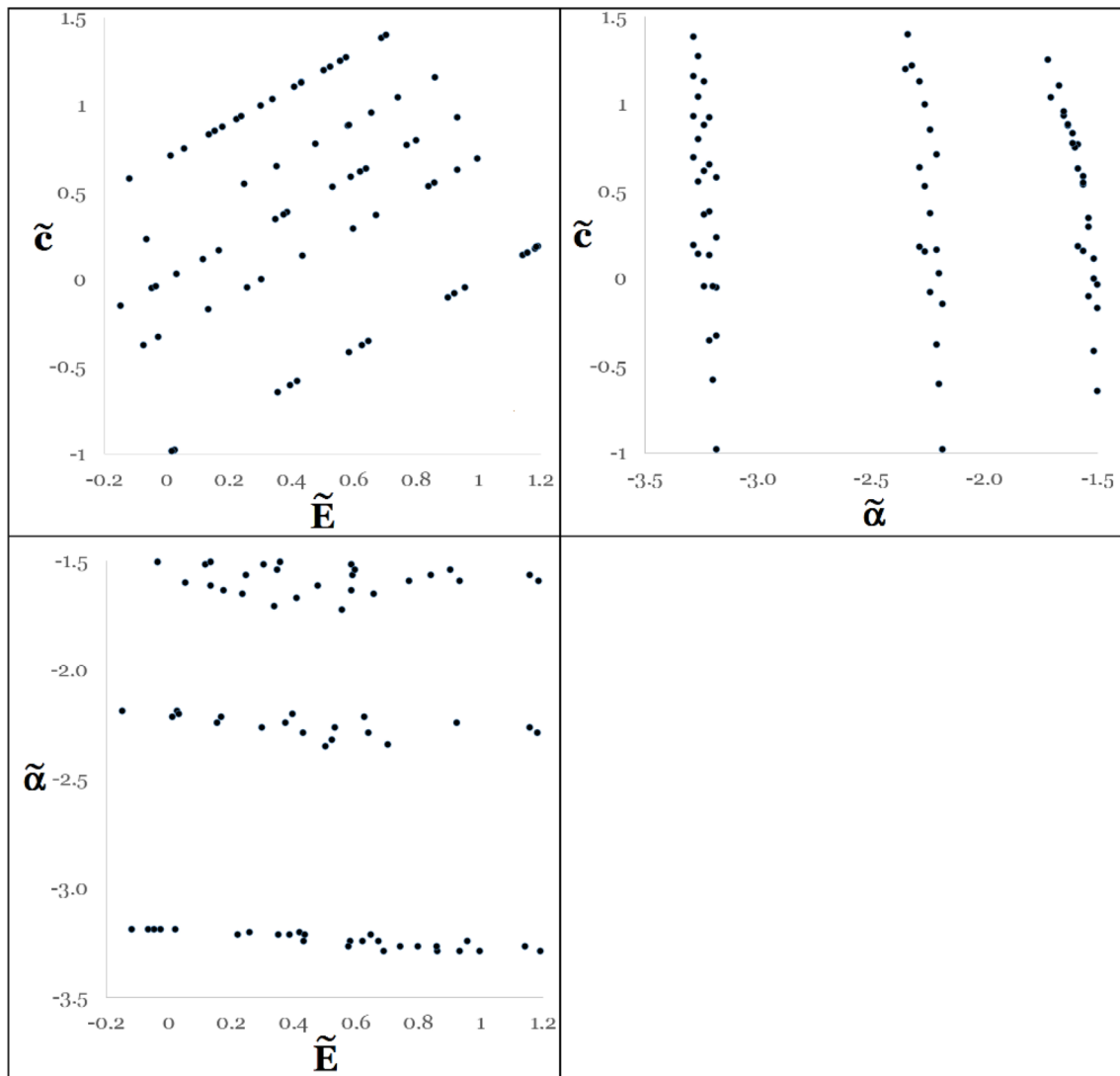


Fig. 3 Normalized parametric space of the mechanical properties of the third-body grains, and location of the 75 simulation points

the maximum value obtained in the numerical campaign). Simulations B, D, E, F, and G were chosen because they frame the case C in a convenient way: the path B–C–D follows a decreasing stiffness (\tilde{c} and $\tilde{\alpha}$ remaining almost constant), the path E–C–F follows an increasing cohesion (\tilde{E} and $\tilde{\alpha}$ remaining almost constant), and the path G–C follows an increasing viscosity (\tilde{c} and \tilde{E} remaining almost constant). All the results presented in this subsection regarding these seven simulations are illustrated by animated views of the relevant fields in the supplementary video provided with this paper.

3.2.1 Simulation A: Very Low Friction Case

Case A corresponds to low values of \tilde{E} and \tilde{c} , meaning that the third body in this case is particularly soft and

slippery. The average friction coefficient in this case is 0.16. A complete description of the flow regime in this case is proposed in Fig. 6, including snapshots of the flow patterns, of the von Mises stress field and of the local strain rate field. This field was computed following the method detailed in [39], and normalized by the global strain rate of the simulation. This figure also provides average velocity profiles, both horizontal and vertical, including their standard deviations, and the friction time series. From Fig. 6, it is clear that low values of \tilde{E} and \tilde{c} lead to a dense layer of compacted third body with no porosity. No clear stress pattern seems to appear, meaning that the load transmission between the first bodies is very homogeneous. The strain rate patterns show mostly horizontal localizations, limited in extension, meaning that the flow regime is mostly laminar. This is confirmed by the velocity

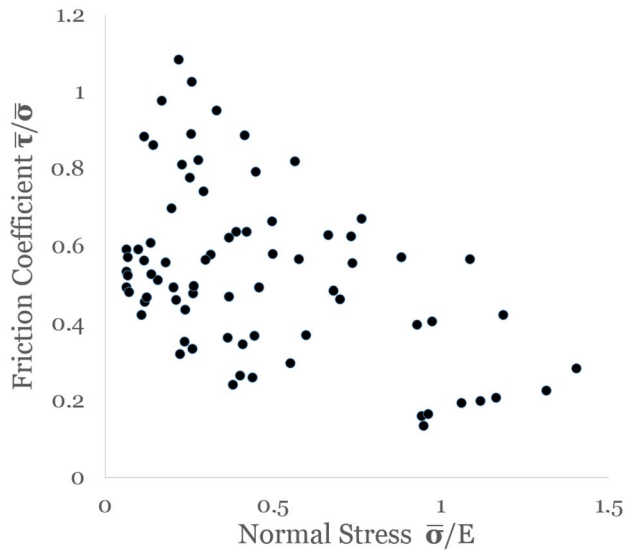


Fig. 4 Time-averaged friction coefficients for all the performed simulations

profiles, which show very limited vertical velocities, and a gradient of horizontal velocity with a trend to shear localization in the central part of the layer. The friction signal remains low and constant. The regime in this case can thus be described as a laminar and localized plastic flow.

3.2.2 Simulations B, C, and D: Influence of the Grains Stiffness

Figures 7, 8, and 9 provide descriptions of the flow regimes of cases B, C, and D, respectively. These three cases follow a path of decreasing values of \tilde{E} (the other parameters being almost constant), which crosses a point of maximum friction (case C). In case B (Fig. 7), one finds a typical granular and cohesive rheology, which was to be expected for such relatively high values of the normalized stiffness. Grains mostly keep their initial circular shapes. The stress fields exhibit the classical inclined force chains. These chains are very commonly observed in the field of granular mechanics, see e.g. [41]. They imply that the force transmission between the first bodies is strongly fluctuating in both space and time. Strain rate patterns show that the grains are only submitted to moderate deformations (blue patches), while most of the velocity jump between the first bodies is accommodated by interparticle motions (yellow patches). The horizontal velocity profile is a rather undisturbed Couette flow with a constant shear rate in the thickness, accompanied by moderate vertical motions. In good agreement with the stress patterns, the friction signal is extremely noisy, with an average value of 0.56 but short peaks up to 1.5, corresponding to formation and collapse of strong percolating force chains. It is likely that if a much wider sample was considered (say

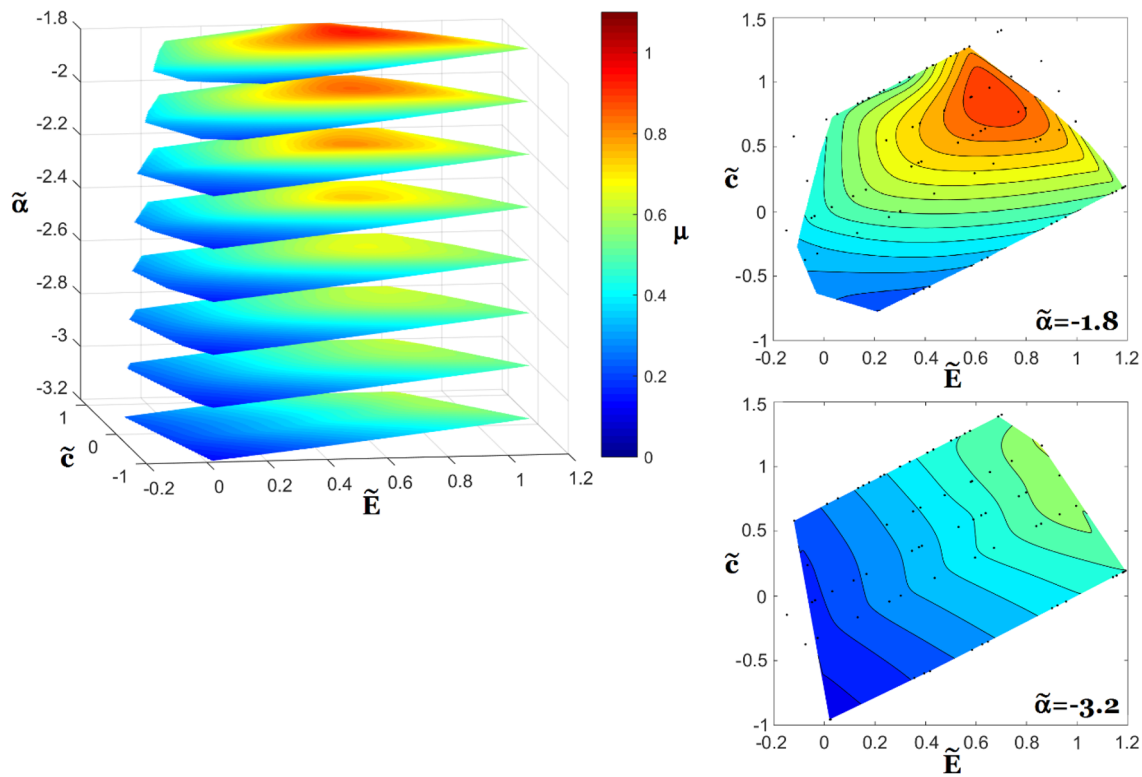


Fig. 5 Mapping of the friction coefficient in the whole parametric space (interpolated between the simulation points)

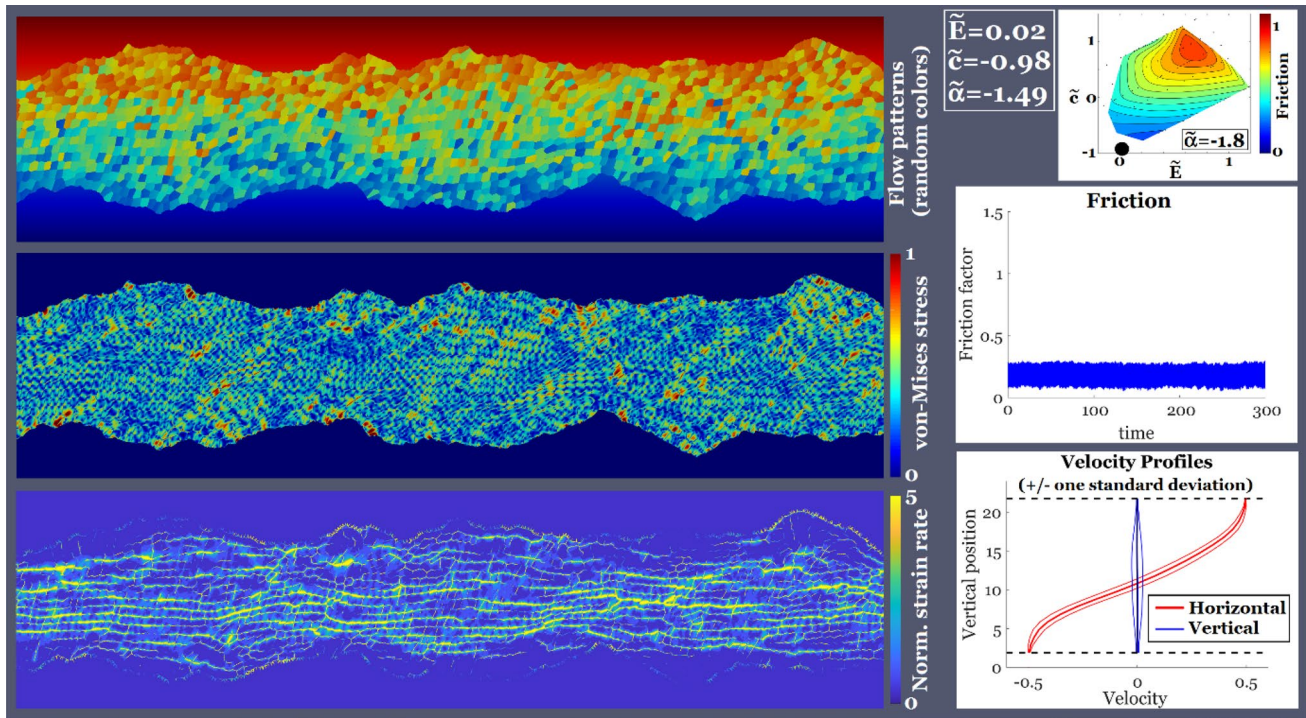


Fig. 6 Flow regime for the simulation A (coefficient of friction equal to 0.16); left-hand side, from top to bottom: snapshots of flow patterns (arbitrary colours), of the von Mises stress field, and of the normalized strain rate field (computed using the technique developed in [34], the value of 1 corresponding here to the constant strain rate

applied at the first bodies); right-hand side, from top to bottom: location of the simulation in the parametric space, friction signal in time, and horizontal and vertical velocity profiles along the thickness of the layer (average in time and horizontal direction, \pm one standard deviation)

ten times wider, for example), these fluctuations would be much more spatially averaged, and their amplitude would be much reduced (because the destruction of the chains at a given location would be compensated by the creation of new chains at another location at the same time). Hence, such fluctuations are a very local phenomenon, which can hardly be verified experimentally since no sensor is currently able to provide such local normal and tangential forces time series. Based on all those observations, the flow regime can be described as a dry granular Couette flow.

The case C (Fig. 8) corresponds to a reduction in \tilde{E} with respect to the case B. This leads to a quite different regime, in the sense that the grains are now well deformed (they are elongated and mostly oriented in the direction of the minor principal stress) and seem to form structured agglomerates with a preferred inclined orientation in the direction of the major principal stress. The stress field reflects this observation and shows the presence of force chains which seem much thicker and stronger than in case B. These structures will hereafter be referred to as “force pillars”. The local strain rate snapshot of Fig. 8 also shows that these agglomerates exhibit limited deformations during the shear and that most of the velocity jump is accommodated by fractures on their inclined contours. It tends to indicate that these force

chains are much more persistent in time than in case B. This is confirmed by the friction signal, which fluctuates much less than in case B but shows a very high average friction of 1.02. The velocity profiles show a strong perturbation of the Couette flow, with a large variability of the horizontal velocity and large vertical velocities as well. This regime can be described as a self-structured agglomerated regime and leads to a maximization of friction.

Figure 9 shows the flow regime for case D, for which the value of \tilde{E} was decreased again. In that case, the third-body grains tend to form very large agglomerates, with a typical size close to the gap distance D of the contact, and a very large porosity. These agglomerates accommodate the velocity jump between the first bodies by a combination of rolling, shearing, separation, and reformation. No more organized force structures do seem to appear in the stress field snapshot, and the local strain rate snapshot shows that the bulk of these large agglomerates remains rather undisturbed and that most of the deformations take place at their boundaries or along specific path in their bulk where fractures propagate for imminent separation. The velocity profiles are much less disturbed than in case C, and the friction signal shows an average value of 0.56 with moderate fluctuations. This is in good agreement with the absence of force chains. Hence,

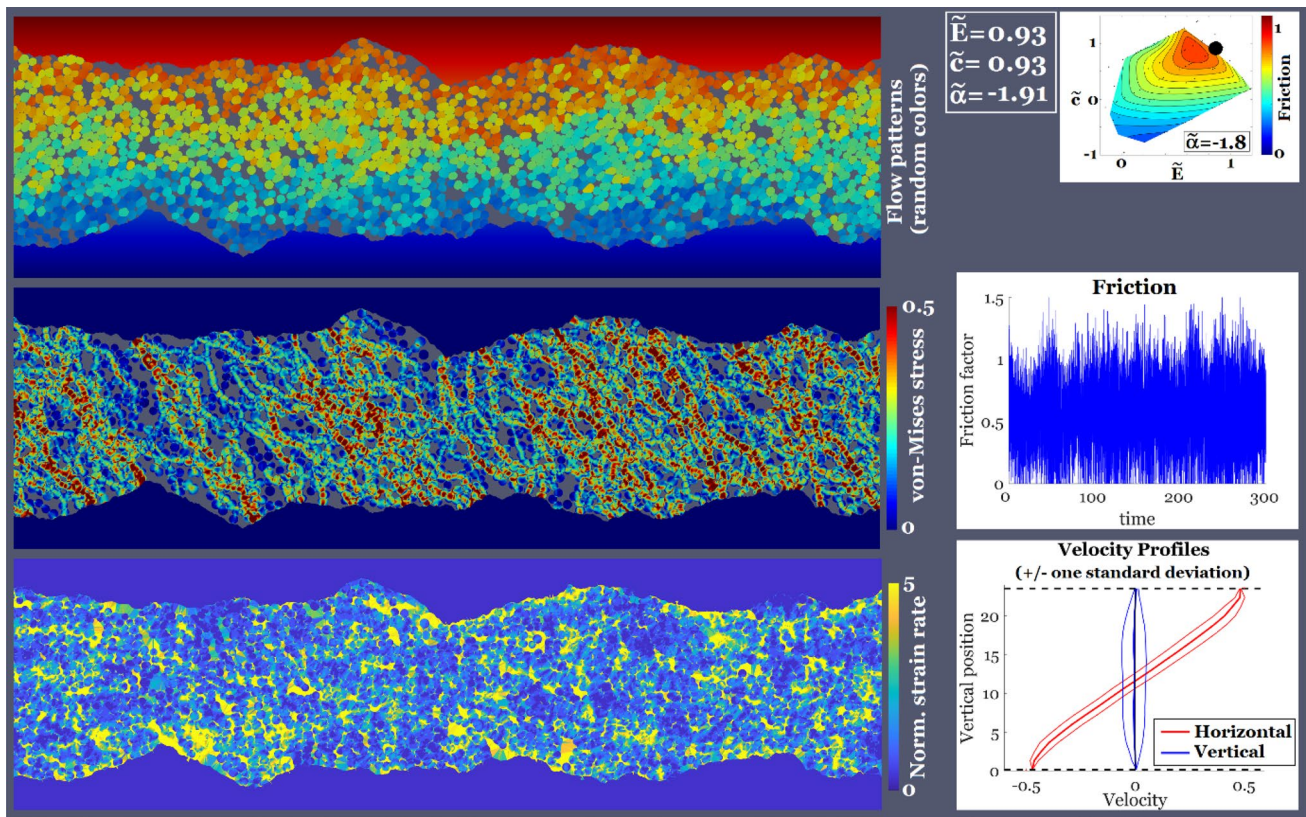


Fig. 7 Flow regime for the simulation B (coefficient of friction equal to 0.56)

this flow can be described as a regime of rolling and shearing of large and soft agglomerates.

3.2.3 Simulations E and F: Influence of the Grains Cohesion

The simulations E–C–F follow a path of increasing cohesion (the other parameters being almost constant), crossing once again a point of maximum friction (case C). The case E (Fig. 10) is rather similar to case A, but with higher levels of \tilde{E} and \tilde{c} . Hence, the very smooth flow regime that was described for case A is here slightly more granular, meaning that the porosity is slightly higher. Some stress patterns seem to appear, although they cannot yet be considered as force chains. The local strain rate patterns are less horizontal, the vertical velocities are slightly larger, and so is the friction coefficient, with an average value of 0.35 and more fluctuations. This situation remains, however, essentially a plastic laminar flow.

When increasing the value of \tilde{c} , we move in the parametric space towards simulation C (Fig. 8), which corresponds to a very high friction and to an agglomerated and structured flow regime. Hence, in this case, an increase in the cohesion between the grains leads to a progressive increase in the formation of intermediate-size agglomerates, to the progressive structuration of these agglomerates in strong force chains,

and to an increase in the friction coefficient. However, if the value of \tilde{c} is still increased beyond the case C, we reach the case F, which is described in Fig. 11. The resulting flow regime appears to be somewhat similar to that of case D, i.e. the formation of large and soft aggregates with a typical size close to the gap D . The major differences lay (i) in the average velocity profiles, exhibiting in case F a plug flow with strong accommodation at the contact between third and first bodies and much larger vertical velocities indicating enhanced mixing, and (ii) in the higher and more strongly fluctuating friction signal. Nevertheless, the average value of friction is equal to 0.82, which is smaller than in case C. Hence, the increase in the normalized cohesion \tilde{c} triggered a change in the flow regime which in turn led to a reduction in the friction.

3.2.4 Simulation G: Influence of the Grains Viscosity

The case G has similar \tilde{c} and \tilde{E} values to case C, but with a much lower value of the normalized viscosity $\tilde{\alpha}$. Figure 12 shows that this decrease in the viscosity has a large influence on the behaviour of the interface. Indeed, the flow patterns do not show the particularly organized structures (i.e. the elongation of the grains along the minor stress direction and formation of agglomerates oriented along the major stress

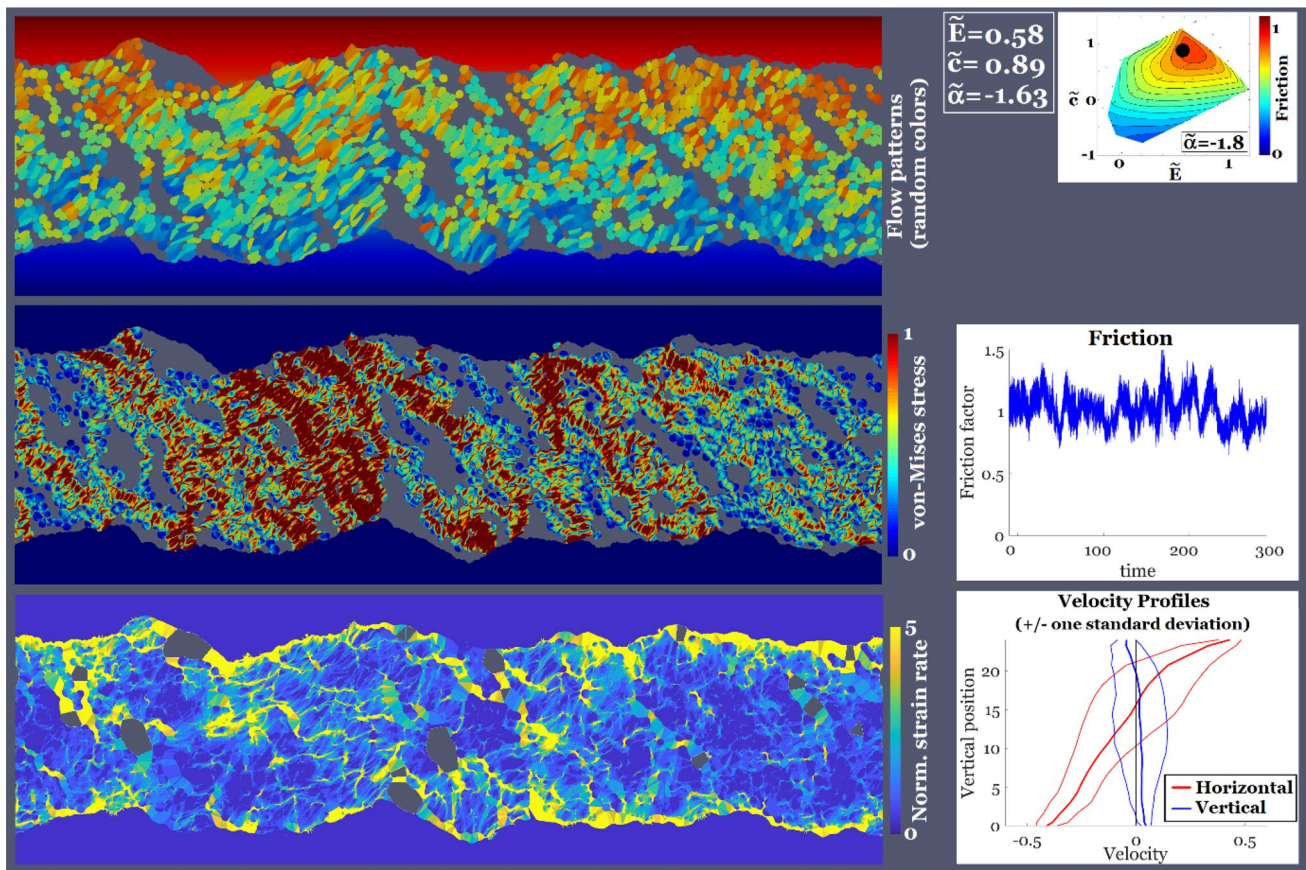


Fig. 8 Flow regime for the simulation C (coefficient of friction equal to 1.02)

direction) and the porosity of case C, but rather a denser packing with moderately deformed grains. The stress field snapshot exhibits more limited patterns of force chains, although they are still present. And the snapshot of the local strain rate field indicates complex accommodation patterns in the form of broad, localized, and mostly sub-horizontal shear bands delimiting intermediate-size agglomerates. The flow regime is a regular Couette flow, and the vertical motions are noticeable but much smaller than in case C. The average value of the friction is pretty low (0.48), but the friction signal is highly fluctuating in a manner similar to case B. Hence, case G is by many aspects similar to the Couette granular flow obtained in case B.

3.3 Local Energy Budget

In the sliding interface simulated in this study, mechanical energy can only be dissipated in two ways: by the Rayleigh damping introduced in the bulk of each deformable grain and by the non-conservative part of the contact laws applied between contacting grains. Hence, one may divide the energy dissipation into two categories:

1. the rate of work done in the bulk of the third-body matter, which represents a proportion p_{wb} of the total dissipation rate. This work is, in this simple model, entirely related to viscous damping, but it can be considered as a proxy for any kind of inelastic behaviour within the bulk of the matter trapped in the interface.
2. the rate of work done at the contacts between grains, which represents a proportion p_{ws} of the total dissipation rate. In the present model, this work is only related to contacts between bodies with a clear contour, but it can be considered as a proxy for any energy-related phenomenon related to surface area creation/destruction within the third-body layer.

The values of p_{wb} obtained for all the simulations of the present study and interpolated in the parametric space are plotted in Fig. 13 as a function of \tilde{c} and with a colour map corresponding to \tilde{E} . p_{wb} is expressed in %, keeping in mind that $p_{wb} + p_{ws} = 100\%$. This figure indicates a very clear dependency of p_{wb} to both \tilde{c} and \tilde{E} . More specifically, it seems that the proportion of bulk dissipation increases linearly with \tilde{c} , with an additional monotonous (negative) contribution of \tilde{E} . The viscosity $\tilde{\alpha}$ does not seem to have

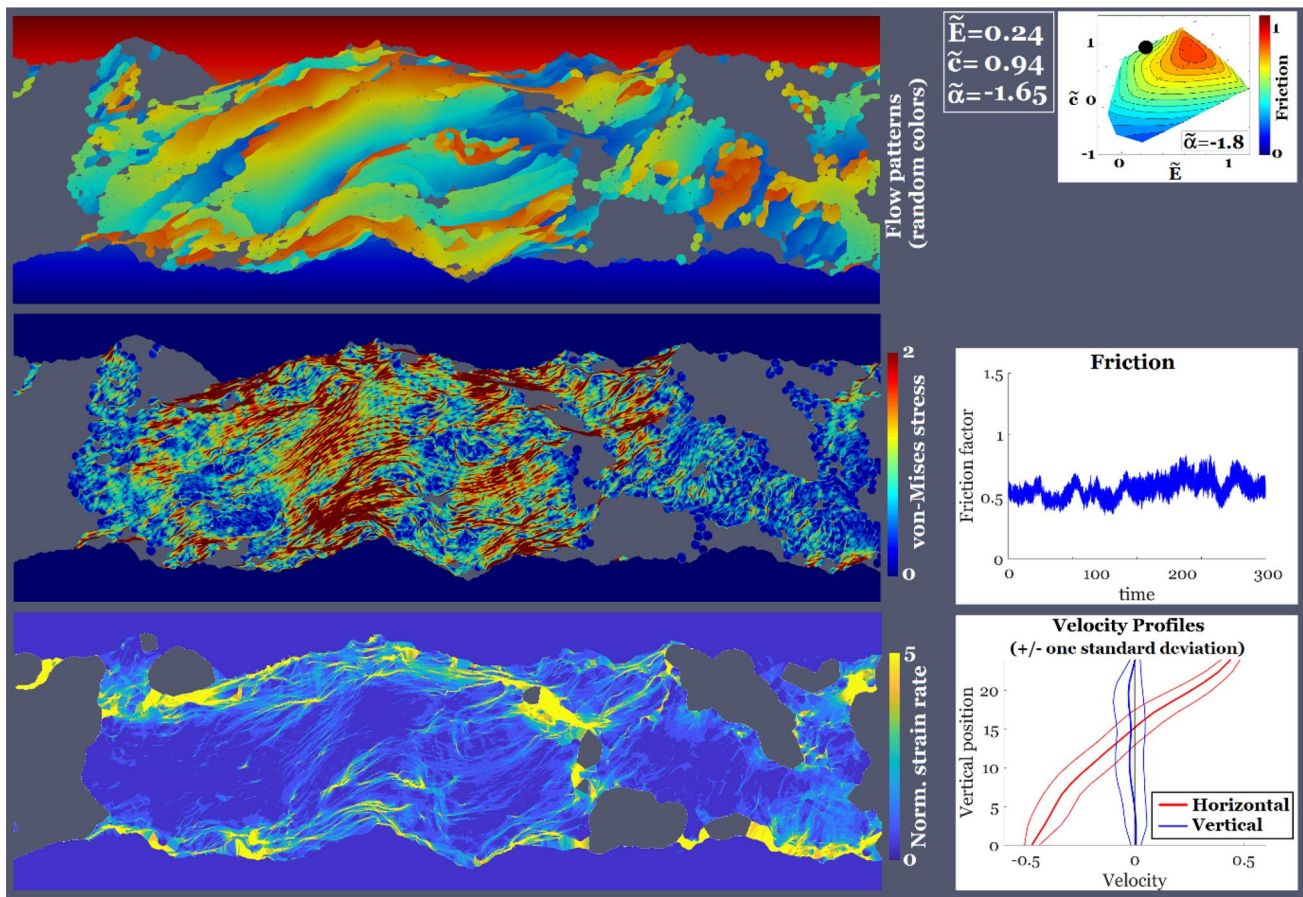


Fig. 9 Flow regime for the simulation D (coefficient of friction equal to 0.56)

a systematic influence on this local energy budget. It also appears that, in general, most of the energy (i.e. 40% to 95%) is dissipated in the bulk of the third-body solid matter, indicating that the choice of using compliant grains to represent this layer makes a lot of sense from an energetic point of view.

Figure 13 provides information on the way energy is dissipated, but not on the amount of dissipated energy. Since the friction coefficient μ is proportional to the total rate of energy dissipation in the system, a convenient way to represent this information is to define partial coefficients of friction μ_b and μ_s , with the following formula:

$$\mu_b = p_{wb} \cdot \mu \tag{5}$$

$$\mu_s = p_{ws} \cdot \mu \tag{6}$$

These quantities provide an additive decomposition of the friction of the form $\mu_b + \mu_s = \mu$ and are mapped in the whole parametric space in Fig. 14. The bulk friction μ_b takes values between 0 and 0.9, while the surface friction μ_s remains between 0 and 0.3. These two components do not seem to be correlated at all, and exhibit complex functional dependencies to the parameters \tilde{E} , \tilde{c} , and $\tilde{\alpha}$. However, a closer look at

Fig. 14 allows to conclude that, roughly speaking, the bulk friction μ_b is mostly controlled by \tilde{c} , that the surface friction μ_s is mostly controlled by \tilde{E} , and that both of them increase monotonically with $\tilde{\alpha}$.

4 Discussion

4.1 The Role of Mesostructures

The results presented in the previous section draw a complex picture of the modes of accommodation within a dry sliding interface in the presence of a third body. An important point is that, within rather simple assumptions (a third body composed of a large number of adhesive, incompressible, viscoelastic bodies), the proposed model returns reasonable values of the friction coefficient and a wide variety of flow regimes which appear consistent with *post-mortem* observations of mature contacts. Although a comprehensive morphological comparison with such experimental observations is out of the scope of the present paper, it certainly represents a promising topic for future studies.

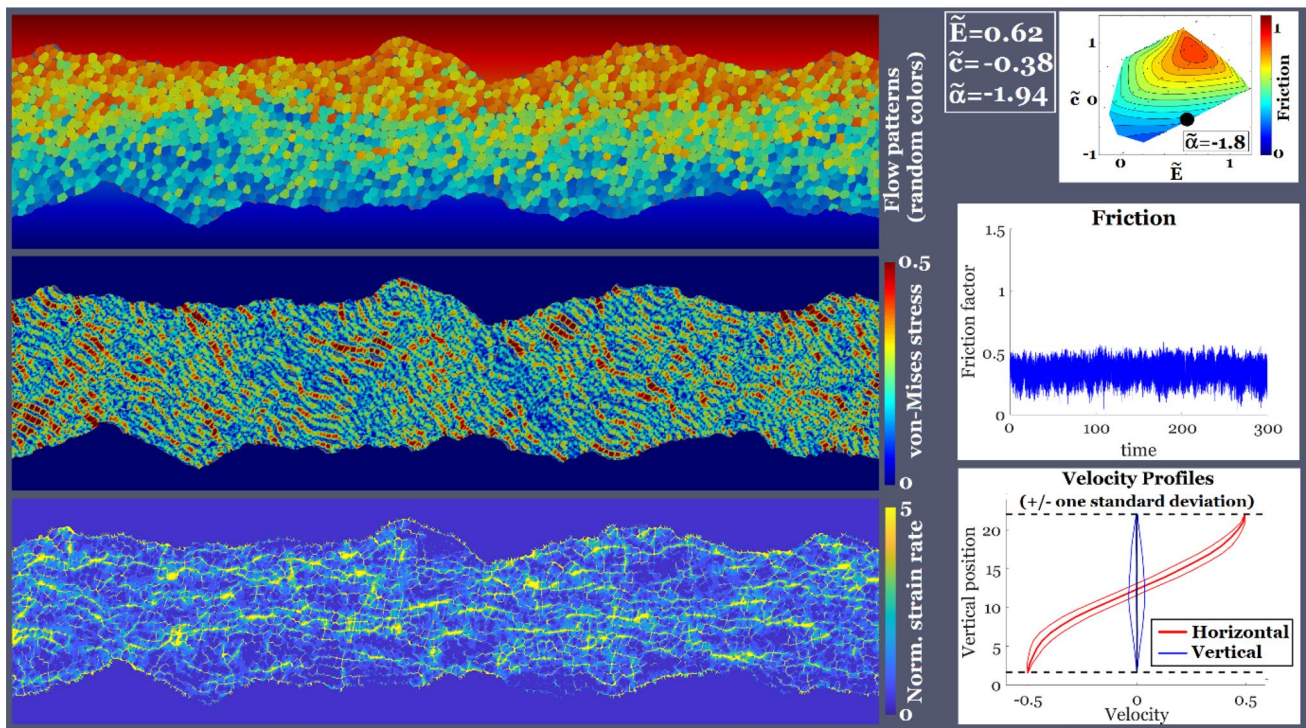


Fig. 10 Flow regime for the simulation E (coefficient of friction equal to 0.35)

Figure 15 shows local snapshots of eight simulations for various values of \tilde{E} and \tilde{c} , and for a quasi-constant value of $\tilde{\alpha}$ close to -1.8 . It thus provides visual information about the interplay between stiffness and cohesion of the grains and gives some clues to understand the different possible flow regimes. Eight different points in the parametric space are observed. Six of them (noted A to F) correspond to regimes analysed in the previous section and two of them (noted H and I) are provided in addition. A quick comparison between cases A, E, and I (or likewise between D, C, and B) shows that an increase in the relative stiffness \tilde{E} tends to decrease the contact area between the grains, with a progressive evolution from a continuous medium with almost no porosity (low values of \tilde{E}) to a granular medium with large porosities (large values of \tilde{E}). At least, this observation holds if one focuses only on the small porosity between neighbouring grains. Case D, for example, shows a very large porosity at the system scale but almost no porosity within the agglomerates, see Fig. 9. Since it is proportional to the contact area, we can conclude that low values of \tilde{E} lead to a larger resistance to sliding and/or separation for any two grains into contact. It can also be inferred that an increase in \tilde{E} leads to an increase in the specific area of the third body.

In contrast, a comparison between cases A, H, and D (or likewise between I and B) indicates that an increase in \tilde{c} seems to bring some structure to the grains patterns. But it does so in different ways, depending on the value of \tilde{E} . On

the one hand, for low values of the relative stiffness (cases A, H, and D), an increase in \tilde{c} tends to increase the deformation of the grains, which get more and more elongated, with a preferred orientation along the minor principal stress. It means that they are submitted to larger shear stresses. On the other hand, for large values of the relative stiffness (cases I and B), an increase in \tilde{c} favours the creation of a network of aligned grains which are likely to promote a larger resistance to shearing (case B), while the third body seems to remain disordered and unstructured if \tilde{c} is low (case I). This spontaneous appearance of “mesostructures” in the third body, i.e. its apparent ability to self-organize when submitted to imposed shear, seems pivotal in the understanding and prediction of dry friction, and possibly wear.

Case C corresponds to a very large value of the average friction (Fig. 8) and represents a trade-off between the different trends described in the two previous paragraphs: for these particular values of \tilde{E} and \tilde{c} , the grains are located along aligned structured, but also exhibit important deformations. Hence, shear strength of the third body in this case arises from both local strength (i.e. large contact areas between grains) and global strength (i.e. structuration of the grains in a resisting network of force pillars). Any change in \tilde{E} or \tilde{c} can only reduce this strength: an increase in \tilde{E} reduces the contact areas between grains (case B), a decrease in \tilde{c} destroys the structuration in chains or pillars (case E), and a decrease in \tilde{E} or an increase in \tilde{c} leads to a complete

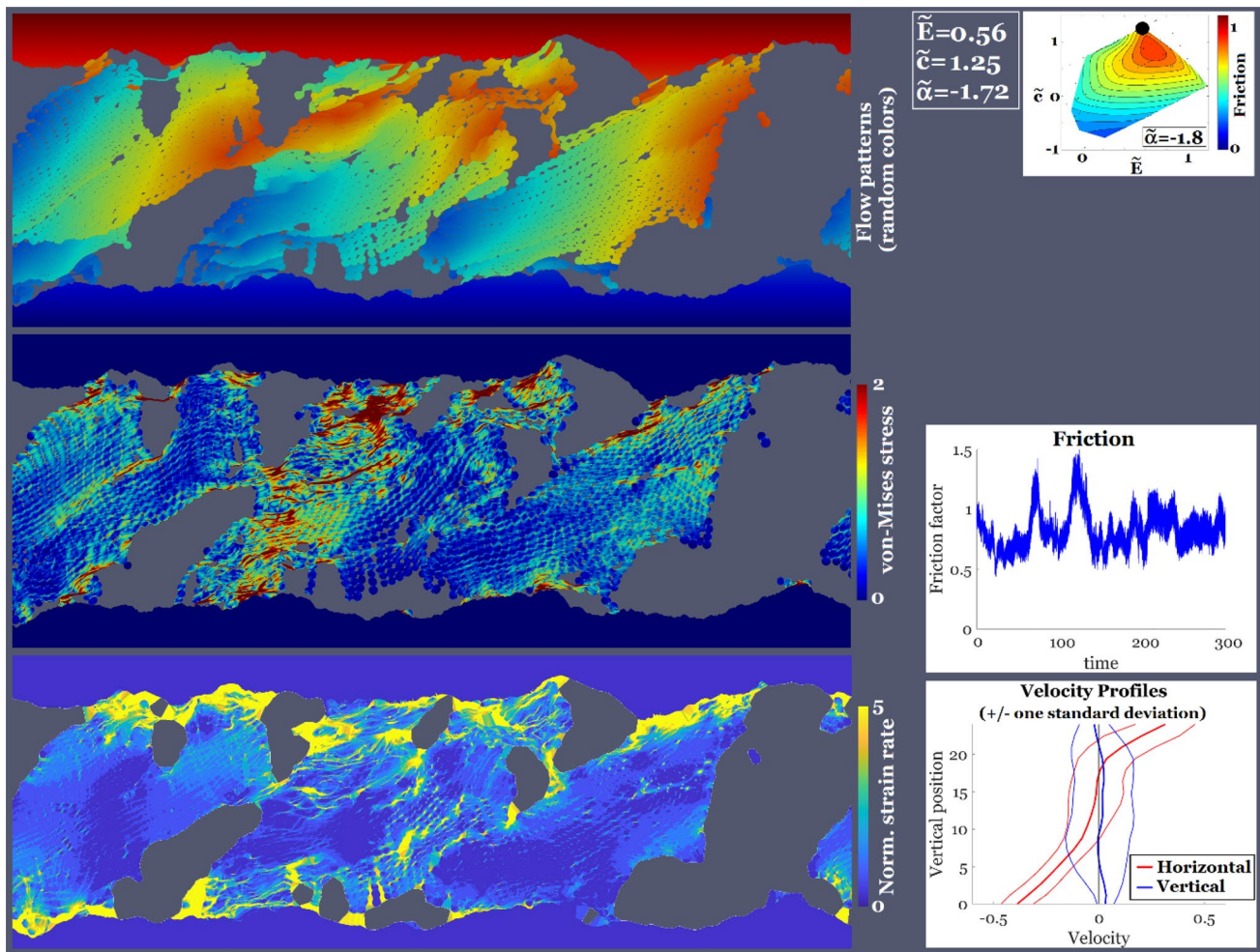


Fig. 11 Flow regime for the simulation F (coefficient of friction equal to 0.82)

agglomeration of the grains (cases D and F) and restrains their mobility, preventing them to form shear-resisting patterns.

From these observations and from the concept of partial friction coefficient introduced in Fig. 14, it is possible to speculate that, for intermediate values of \tilde{c} (i.e. close to 0), an increase in \tilde{E} increases μ_s by reducing the strength of the bonds between grains and thus favouring their mobility and the associated energy dissipation. However, lower values of \tilde{c} attenuate this form of energy dissipation because the inter-particle contacts are too weak to dissipate a lot of energy. Likewise, high values of \tilde{c} induce a drop of μ_s because the bonds between the grains are now too strong to fail, and thus do not dissipate much energy. They in turn activate a large increase in μ_b (Fig. 13) because the velocity accommodation between the first bodies, which has to take place somewhere, is transferred into the bulk of the solid matter composing the third body. Since the points of maximum values of μ_s and μ_b do not coincide in the parametric space. They do not have the same physical explanations. The point of maximum

friction is located somewhere in between, and friction is thus bonded in the parametric space.

4.2 A First Comparison with Experiments

A rigorous quantitative experimental validation of the findings of the present paper will require many further studies and might prove very challenging. However, it is possible to propose a first qualitative estimation of the relevance of the proposed model by a quick comparison with selected results from the literature. This is proposed in Fig. 16, which presents micrographs of wear tracks obtained in state-of-the-art tribometer experiments. Figure 16a–c was taken from [41]. In this study, a copper powder with a grain size smaller than 75 μm was used as an artificial third body in a friction test involving a sintered copper-based friction material. These three figures correspond to an increasing normal load, which corresponds to a decrease in \tilde{E} in the nomenclature of the present paper, assuming that the material deformability remains a constant. This is questionable because thermal effects may

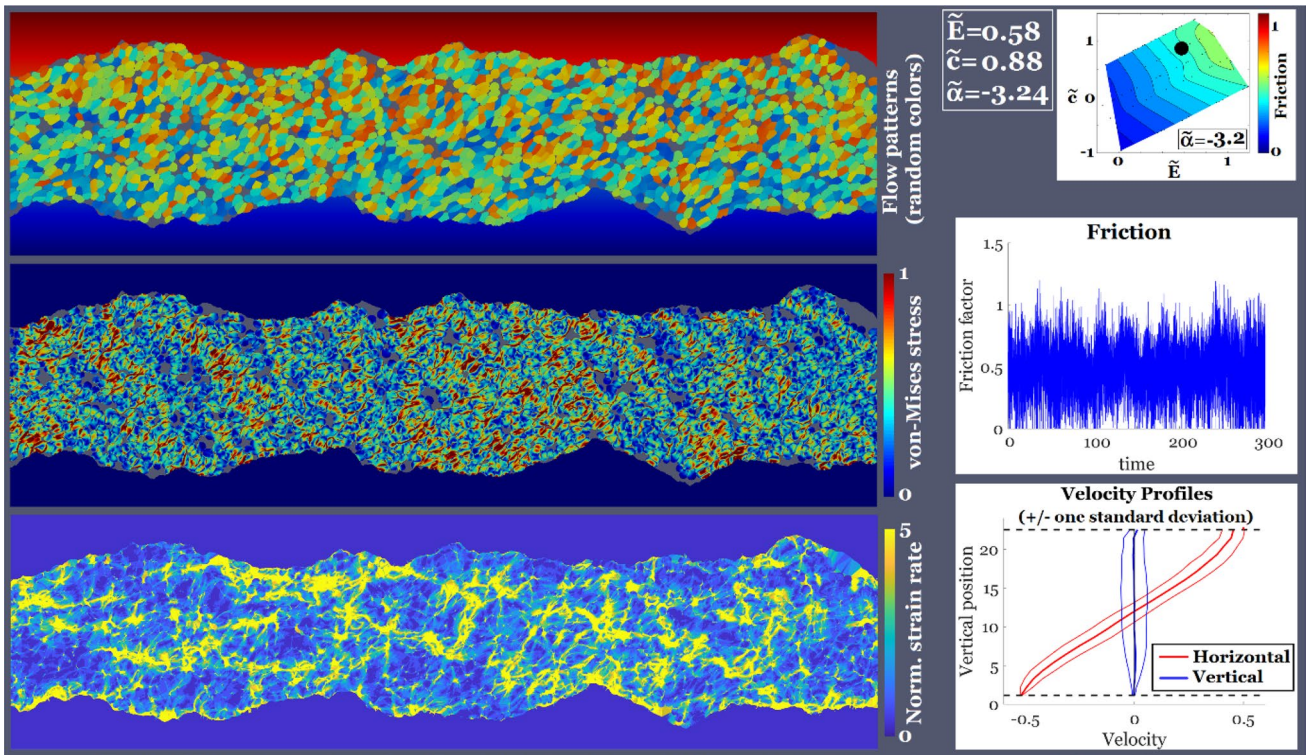


Fig. 12 Flow regime for the simulation G (coefficient of friction equal to 0.48)

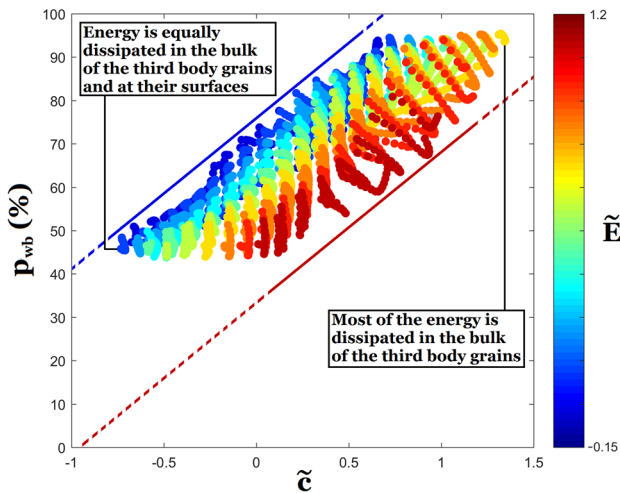


Fig. 13 Proportion of the energy dissipated in the bulk of the solid matter composing the third body, as a function of \tilde{c} (points interpolated in the whole parametric space between the simulation points; dots colours indicate the value of \tilde{E} for the corresponding data points; linear fittings are only provided as a guide for the eye)

increase with the load (since more energy is consumed) and may lead to a softening of the material, but it would only lead to a value of \tilde{E} decreasing even faster with $\tilde{\sigma}_n$. The experimental influence of \tilde{E} on the third-body morphology is pretty

clear: the decrease in \tilde{E} leads to an agglomeration of the grains in larger and larger aggregates, until formation of a continuous layer of third body. Indeed, the third body obtained in the case of Fig. 16a is described in [42] with the terms “plate-like hard metal debris which disperse on the surface”, which is consistent with the granular regime obtained numerically for high values of \tilde{E} . In the situation of Fig. 16b, it is mentioned that “copper powder coheres together”, which is also in good agreement with the formation of larger agglomerates for intermediate values of \tilde{E} . And in the case of Fig. 16c, for which the applied normal pressure is the highest, the layer is described as “more compact” and in a “dense and continuous state”, in the manner of simulations D or H for which the value of \tilde{E} is very low. Thermal effects are the main explanation used in [42] to interpret these morphologies, because of the associated increase in the material deformability, and the truth probably lies in both explanations: an increase in the normal load and a decrease in the stiffness makes the value of \tilde{E} smaller and leads to agglomeration and eventually densification of the third-body layer because of the phenomena described earlier in this paper. It should also be noted that friction coefficients reported in [42] decrease with the decrease in \tilde{E} , which is in good qualitative agreement with the numerical results obtained for low values of $\tilde{\alpha}$ (Fig. 15). This is consistent with the low value of the viscosity of copper reported in [40].

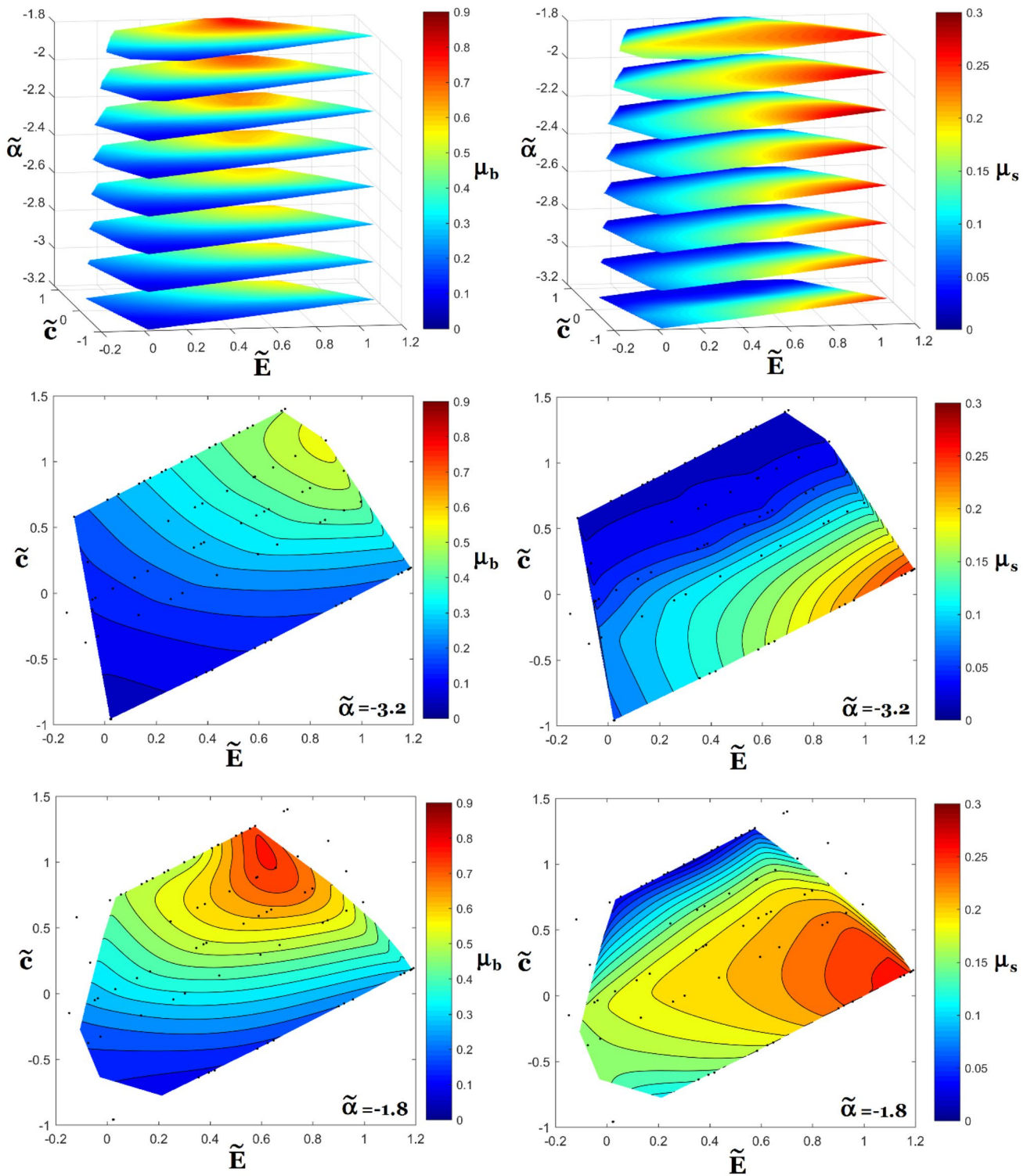


Fig. 14 Partial coefficients of friction related to surface phenomena (creation and destruction of free surfaces and sliding between grains) and to bulk deformation of the third-body solid matter, plotted in the

whole parametric space and for two specific values of $\tilde{\alpha}$ (values interpolated between the simulation points)

Figure 16d, e was taken from [43]. In that study, a Zr-based metallic glass was submitted to wear tests under different chemical environments with a decreasing content

of oxygen. More specifically, Fig. 16d corresponds to a test performed in pure oxygen, while Fig. 16e corresponds to pure argon. This means that the value of \tilde{c} is likely to be

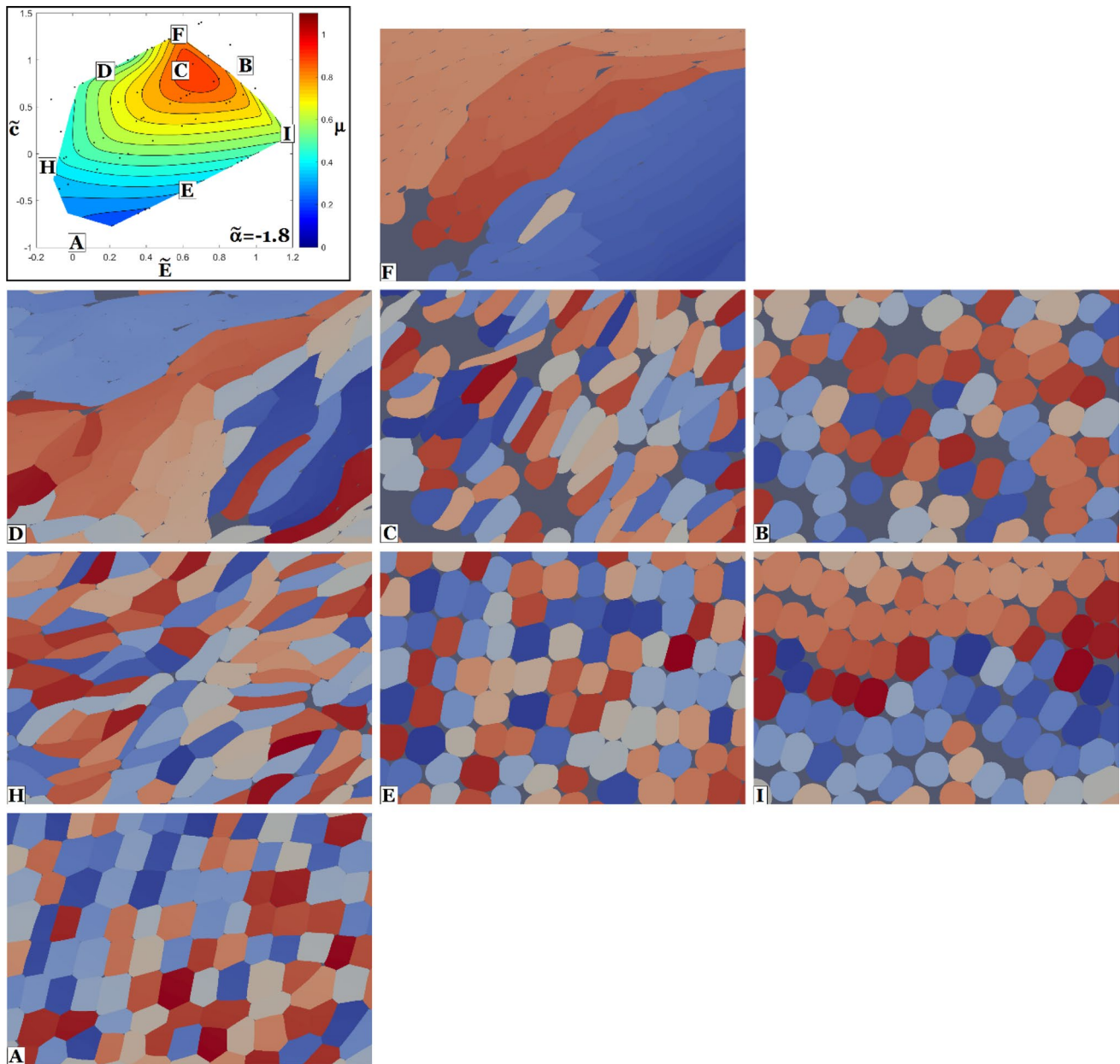


Fig. 15 Local snapshots of third-body microstructures for eight simulations performed at similar values of $\tilde{\alpha}$ (between -1.94 and -1.49)

much lower in the first case than in the second, because argon will inhibit oxidation and preserve the reactivity of newly created surfaces. Figure 16d shows a cross section and a top view of isolated third-body grains, as well as a top view of the wear track. It appears that, in the case of an oxygen-rich environment, the grains are rigid and angular, which is confirmed by signatures of abrasive wear on the wear track. In [43], this third body is described as “abrasive particles”, in accordance with the granular model obtained in simulations for low values of \tilde{c} (provided that \tilde{E} is large enough). On the other hand, Fig. 16e shows a cross section and a top view of a third-body layer

which appears much more continuous and ductile. It is described in [43] as a “mixed layer”, “relatively smooth” with evidences of “plastic deformation”. The influence of \tilde{c} on the third-body flow is thus pretty clear, with a granular behaviour for lower \tilde{c} , and a much more plastic and agglomerated flow for higher \tilde{c} . In the parametric space of Fig. 15, it could correspond to the path E–F, for example. Although these observations do not constitute any proof, they certainly provide a certain amount of confidence in the ability of the proposed numerical model to mimic some realistic solid flow regimes, as observed in tribological experiments. It also shows that a realistic simulation

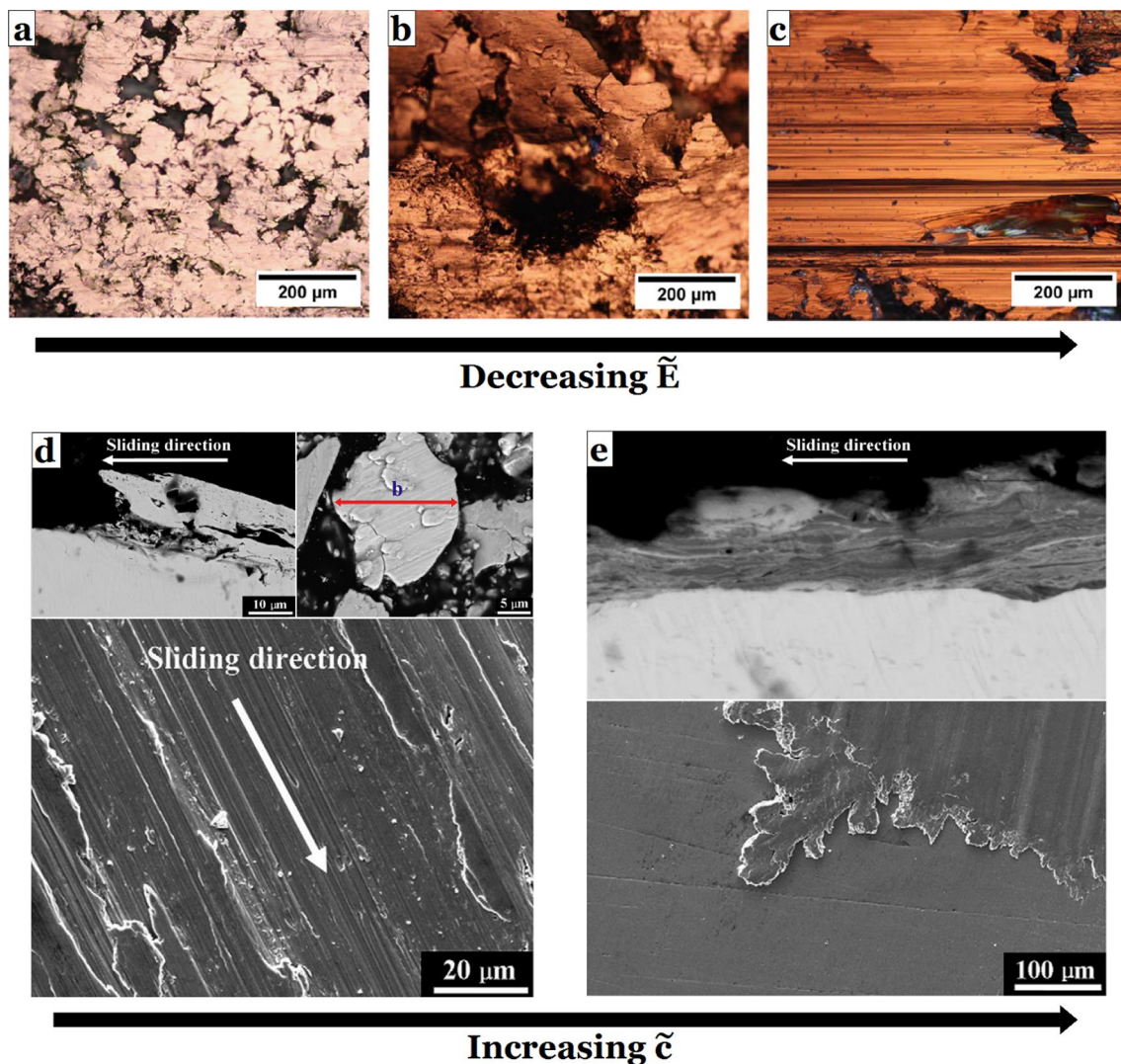


Fig. 16 Examples of third-body morphologies taken from the literature, with single-parameter variations; **a–c** top views of copper powder third body under increasing normal stress (i.e. decreasing \tilde{E}),

taken from [42]; **d, e** cross sections and top views of metallic glass third bodies with decreasing content of oxygen (i.e. increasing \tilde{c}), taken from [43]

of the third-body flow regime might make it possible in future works to understand some associated wear regimes (abrasive wear versus adhesive wear, for example), since the connexion between both aspects is often observed experimentally. A good way to perform such a task would be to make the first bodies deformable, i.e. to allow them to experience stress fields. The exact tribological loading applied by the third body on the surfaces would thus be clarified, and focus could be put on the response of the surfaces to these loadings (microstructural evolution, fatigue, damage, and eventually wear).

4.3 Current Limitations of the Proposed Approach

Because of the local nature of this model, a number of problems could not be addressed. In a real contact, the normal pressure field is not homogeneous in either space and time. The two surfaces are not motion driven but rather are driven by a complex interplay between remote actuators and by the deformability and dynamics of the first bodies. And third body may be transported from one part of the contact to another until possible ejection of the contact and, thus, wear. These phenomena are likely to considerably change the simple picture presented in this paper and to introduce additional energy dissipation modes, and call for a multi-scale analysis. Such important phenomena as stick–slip and acoustic wave emissions require this

additional scale, which is expected to be tackled in a future study, but will require a novel and appropriate numerical framework.

Meanwhile, the local view of the contact proposed in this paper may be largely enriched. A number of parameters were not investigated yet, such as shapes of the grains, thickness of the layer, roughness, adhesion between first and third bodies, and more complex constitutive laws and contact models. A particularly important point is the size distribution of the grains, for several reasons. First, it is likely that the ratio between the grains size and the layer thickness (i.e. the typical number of grains in the thickness) will have consequences on the flow regime. Second, it is commonly observed that smaller grains are stiffer, and this scale dependency might modify the interface behaviour. And third, the whole concept of a “third-body particle” is questionable. Experiments have shown that third bodies are both discontinuous and deformable, which is well captured by a collection of deformable grains, but there is no certainty that such a “grain” is actually an elementary third-body particle, and not an aggregate of smaller elements.

Natural particle breakage and comminution are not considered in this study, and the size of the grains is arbitrary. The energetics of particle breakage mostly lie in the fracture energy, i.e. in the energy required to create new surfaces, and this energy is already present in some of the simulations reported in this paper, when large agglomerates get crushed and form smaller ones. But this kind of breakage can only occur along the contours of the individual grains which form the agglomerate in the first place, and thus remains arbitrary. It is likely that the ability of the grains to fail spontaneously along any path would lead the third body to some sort of steady-state grain size distribution which might be more meaningful than the homogeneous distribution used in the present study. Such important questions will have to be investigated in future studies.

Another interesting perspective would be the implementation of heat production and diffusion within the interface, and appropriate feedback of the temperature field on the mechanical properties of the third body (deformability and cohesion, for example). Indeed, the current simulations are isothermal in the sense that the very concept of temperature does not exist in the current code, and this is a strong limitation. The notion of passivation of the free surfaces of the third body exposed to the gaseous environment might also prove useful. These interesting leads will be followed in future studies, as well as confrontations of this model to experimental observations of morphologies and flows of third bodies in lab conditions.

5 Conclusion

The parametric study presented in this paper provides some insights into the kinematic and energetic phenomena taking place locally within a dry sliding interface in the presence of a third body. Although rather complex in its numerical implementation, this study is based on simple mechanical assumptions on the third-body behaviour. The numerical results indicate that there is an intricate interplay between the deformability, the cohesion, and the viscosity of the matter composing the third body.

The proposed numerical approach makes it possible to observe a large variety of third-body flow regimes, which make sense from an experimental viewpoint but could not appear in simulations at the same scale performed with DEM and previously reported in the literature, because of a too restrictive set of assumptions (essentially, the fact that grains remain rigid in traditional DEM).

Emerging values of the coefficient of friction are reasonable for dry friction, for a wide class of physical properties of the third body, including very cohesive ones. It is related to the fact that the third body leads to a self-limitation of friction, thanks to its ability to adapt its flow regime in order to minimize the local energy consumption in the contact. The maximum value that the friction coefficient can take in the presence of a third body is slightly larger than one, which is consistent with experimental knowledge in common tribological practice. While the classical explanation for this experimental fact relies on the concept of asperities and of a real contact area (and thus implies rough and clean surfaces and requires to consider the entire contact), we show in this paper that, in the presence of a third body, this range of values for μ is explained by locally self-limiting dissipation modes which rely on flow regimes evolutions.

The link between the flow regime and the friction coefficient is based on the ability (or not) of the third body to build mesostructures at an intermediate scale in order to oppose to sliding: force chains, force pillars, small-size agglomerates, large-size agglomerates, etc. In turn, this ability is strongly related to the mechanical properties of each third-body grain, especially on its stiffness (allowing it to deform and to adapt its shape to its surroundings, possibly maximizing its contact surface with its neighbours and preventing it to slip or rotate) and on its cohesion (allowing it to build strong links with its neighbours and preventing relative motions).

An analysis of the energetics of the mechanical processes in the sheared third bodies shows that an increased stiffness favours energy dissipations by surface-related phenomena (i.e. fracture energy consumption by creation of new surfaces), while an increased cohesion activates

energy dissipation by inelastic phenomena during bulk deformation of the matter composing the third-body particles. The role of viscosity is more complex, but it seems to increase the relaxation time and to lead the grains to keep their shape longer (and thus to increase the life duration of mesostructures). A larger viscosity thus systematically increases the friction coefficient.

Future studies may make it possible to clarify the role of third-body mesostructures in the friction and to investigate their effects on wear, in relation to experimental works. The local view of the contact presented in this paper will be enriched by additional physics (grains plasticity, comminution, heat production and flow, etc.) and completed by connections with the upper scales of the tribological triplet.

Compliance with Ethical Standards

Conflict of interest The author acknowledges that this study contains original material, as a result of a purely academic study without any kind of private funding or conflict of interest. Its publication has been approved tacitly by the responsible authorities at the institute where the work has been carried out.

References

- Kounoudji, K., Renouf, M., Mollon, G., Berthier, Y.: Role of third body on bolted joints' self-loosening. *Tribol. Lett.* **61**, 25 (2016)
- Scholtz, C.H.: *The mechanics of earthquakes and faulting*, 2nd edn. Cambridge University Press, Cambridge (2012)
- Pastewka, L., Prodanov, N., Lorenz, B., Müser, M.H., Robbins, M.O., Persson, B.N.J.: Finite-size scaling in the interfacial stiffness of rough elastic contacts. *Phys. Rev. E* **87**(6), 062809 (2013)
- Luan, B.Q., Hyun, S., Molinari, J.-F., Berstein, N., Robbins, M.O.: Multiscale modeling of two-dimensional contacts. *Phys. Rev. E* **74**, 046710 (2006)
- Dieterich, J., Kilgore, B.D.: Imaging surface contacts: power law contact distributions and contact stresses in quartz, calcite, glass, and acrylic plastic. *Tectonophysics* **256**, 219–239 (1996)
- Yastrebov, V.A., Anciaux, G., Molinari, J.-F.: Contact between representative rough surfaces. *Phys. Rev. E* **86**, 035601 (2012)
- Bowden, F.P., Tabor, D.: *The friction and lubrication of solids*. Oxford University Press, Oxford (1950)
- Berthier, Y.: Experimental evidence for friction and wear modeling. *Wear* **139**, 77–92 (1990)
- Jacq, C., Nelias, D., Lormand, G., Girodin, D.: Development of a three-dimensional semi-analytical elastic-plastic contact code. *J. Tribol.* **124**(4), 653–667 (2002)
- Tsala, S., Berthier, Y., Mollon, G., Bertinotti, A.: Numerical analysis of the contact pressure in a quasi-static elastomeric reciprocating sealing system. *J. Tribol.* **140**, 064502-1 (2018)
- Saulot, A., Baillet, L.: Dynamic finite element simulations for understanding wheel-rail contact oscillatory states occurring under sliding conditions. *J. Tribol.* **128**, 761–770 (2006)
- Fagiani, R., Barbieri, M.: Modelling of finger-surface contact dynamics. *Tribol. Int.* **74**, 130–137 (2014)
- Berthier, Y., Descartes, S., Busquet, M., Niccolini, E., Desrayaud, C., Baillet, L., Baietto-Dubourg, M.C.: The role and effects of the third body in the wheel–rail interaction. *Fatigue Fract. Eng. Mater. Struct.* **2004**(27), 423–436 (2004)
- Godet, M.: The third-body approach: a mechanical view of wear. *Wear* **100**, 437–452 (1984)
- Colas, G., Saulot, A., Godeau, C., Michel, Y., Berthier, Y.: Describing third body flows to solve dry lubrication issue—MoS₂ case study under ultrahigh vacuum. *Wear* **305**(1–2), 192–204 (2013)
- Elrod, H.G., Brewe, D.E.: Numerical experiments with flows of elongated granules. *Tribol. Ser.* **21**, 219–226 (1991)
- Seve, B., Iordanoff, I., Berthier, Y.: A discrete solid third body model: influence of the intergranular forces on the macroscopic behavior. *Tribol. Interface Eng. Ser.* **39**, 361–368 (2001)
- Fillot, N., Iordanoff, I., Berthier, Y.: Simulation of wear through a mass balance in a dry contact. *ASME J. Tribol.* **127**(1), 230–237 (2005)
- Renouf, M., Fillot, N.: Coupling electrical and mechanical effects in discrete element simulations. *Int. J. Numer. Methods Eng.* **74**, 238–254 (2008)
- Mollon, G.: A numerical framework for discrete modelling of friction and wear using Voronoi polyhedrons. *Tribol. Int.* **90**, 343–355 (2015)
- Renouf, M., Massi, F., Fillot, N., Saulot, A.: Numerical tribology of a dry contact. *Tribol. Int.* **44**, 834–844 (2011)
- Cundall, P.A., Strack, O.D.L.: A discrete numerical model for granular assemblies. *Géotechnique* **29**(1), 47–65 (1979)
- Ghaboussi, J., Barbosa, R.: Three-dimensional discrete element method for granular materials. *Int. J. Numer. Anal. Meth. Geomech.* **14**, 451–472 (1990)
- Tsounngui, O., Vallet, D., Charmet, J.C.: Numerical model of crushing of grains inside two-dimensional granular materials. *Powder Technol.* **105**, 190–198 (1999)
- Donze, F.V., Richefeu, V., Magnier, S.A.: Advances in discrete element method applied to soil, rock and concrete mechanics. *Electr. J. Geotechn. Eng.* **8**, 44 (2009)
- Mollon, G., Richefeu, V., Villard, P., Daudon, D.: Discrete modelling of rock avalanches: sensitivity to block and slope geometries. *Granul. Matter* **17**(5), 645–666 (2015)
- Renouf, M., Cao, H.-P., Nhu, V.-H.: Multiphysical modeling of third-body rheology. *Tribol. Int.* **44**, 417–425 (2011)
- Champagne, M., Renouf, M., Berthier, Y.: Modeling wear for heterogeneous bi-phasic materials using discrete elements approach. *ASME J. Tribol.* **136**(2), 021603 (2014)
- Da Cruz, F., Emam, S., Prochnow, M., Roux, J.-N., Chevoir, F.: Rheophysics of dense granular materials: discrete simulation of plane shear flows. *Phys. Rev. E* **72**, 021309 (2005)
- Coussot, P., Ancey, G.: Rheophysical classification of concentrated suspensions and granular pastes. *Phys. Rev. E* **59**(4), 4445 (1999)
- Mollon, G., Zhao, J.: 3D generation of realistic granular samples based on random fields theory and Fourier shape descriptors. *Comput. Methods Appl. Mech. Eng.* **279**, 46–65 (2014)
- Azema, E., Radjai, F., Saussine, G.: Quasistatic rheology, force transmission and fabric properties of a packing of irregular polyhedral particles. *Mech. Mater.* **41**, 729–741 (2009)
- Harthong, B., Jerier, J.-F., Richefeu, V., Chareyre, B., Doremus, P., Imbault, D., Donzé, F.-V.: Contact impingement in packings of elastic-plastic spheres, application to powder compaction. *Int. J. Mech. Sci.* **61**, 32–43 (2012)
- Gustafsson, G., Haggblad, H.-A., Jonsen, P.: Multi-particle finite element modelling of the compression of iron pellets with statistically distributed geometric and material data. *Powder Technol.* **239**, 231–238 (2013)
- Nayroles, B., Touzot, G., Villon, P.: Generalizing the finite element method: diffuse approximation and diffuse elements. *Comput. Mech.* **10**, 307–318 (1992)

36. Belytschko, T., Lu, Y.Y., Gu, L.: Element-free Galerkin methods. *Int. J. Numer. Meth. Eng.* **37**, 229–256 (1994)
37. Mollon, G.: A multibody meshfree strategy for the simulation of highly deformable granular materials. *Int. J. Numer. Meth. Eng.* **108**(12), 1477–1497 (2016)
38. Mollon, G.: A unified numerical framework for rigid and compliant granular materials. *Comput. Part. Mech.* **5**(4), 517–527 (2018)
39. Mollon, G.: Mixtures of hard and soft grains: micromechanical behavior at large strains. *Granul. Matter* **20**, 39 (2018)
40. Savenkov, G.G., Meshcheryakov, Y.I.: Structural viscosity of solids. *Combust. Explos. Shock Waves* **38**(3), 352–357 (2002)
41. Zhang, J., Majmudar, T., Behringer, R.: Force chains in a two-dimensional granular pure shear experiment. *Chaos* **18**, 041107 (2008)
42. Su, L., Gao, F., Han, X., Chen, J.: Effect of copper powder third body on tribological property of copper-based friction material. *Tribol. Int.* **90**, 420–425 (2015)
43. Wu, H., Baker, I., Liu, Y., Wu, X., Munroe, P.R.: Effects of environment on the sliding tribological behaviors of Zr-based bulk metallic glass. *Intermetallics* **25**, 115–125 (2012)

Publisher's Note Springer Nature remains neutral with regard to jurisdictional claims in published maps and institutional affiliations.